Available online at www.sciencedirect.com

SciVerse ScienceDirect

Ceramics International 39 (2013) 1011–1019

CERAMICS INTERNATIONAL

www.elsevier.com/locate/ceramint

# From AgI/$TiO_2$ to Ag/$TiO_2$: effects of the annealing temperature on the compositions, porous nanostructures, and visible-light photocatalytic properties

Juzheng Zhang[a], Xin Liu[a], Shanmin Gao[a,b,*], Baibiao Huang[b,**], Ying Dai[b], Yanbin Xu[a], Lauren R. Grabstanowicz[c], Tao Xu[c]

[a]School of Chemistry and Materials Science, Ludong University, Yantai 264025, China
[b]State Key Labs of Crystal Materials, Shandong University, Jinan 250100, China
[c]Department of Chemistry and Biochemistry, Northern Illinois University, DeKalb, IL 60115, USA

Received 5 April 2012; received in revised form 20 June 2012; accepted 5 July 2012
Available online 14 July 2012

**Abstract**

AgI/$TiO_2$ and Ag/$TiO_2$ porous nanostructures were synthesized using $AgNO_3$, KI, thioglycollic acid, and tetrabutyl orthotitanate as a precursor. AgI nanoparticles were used as seeds to initiate the nucleation of a precursor $TiO_2$ shell, and thioglycollic acid acted as a hydrolysis inhibitor and porosity promoter. The hybridized samples were annealed at different temperatures. Porous AgI/$TiO_2$ nanostructures were formed at low annealing temperatures (300 and 400 °C). At 600 °C, the porous Ag/$TiO_2$ nanostructures exhibited a plasmon resonance effect. The formation mechanism of the different porous nanostructures was also investigated. Methylene blue solutions were used as wastewater to evaluate the visible-light photocatalytic activity of the samples. The porous nanostructured photocatalyst exhibited substantially high visible-light-induced photocatalytic activity for the photodegradation of methylene blue compared with pristine AgI and $TiO_2$ nanoparticles.


*Keywords:* A. Powders: chemical preparation; B. Nanocomposites; D. $TiO_2$; Photocatalytic chemistry

## 1. Introduction

The excellent chemical stability, nontoxicity, and photoactivity of $TiO_2$ has attracted considerable attention and indicated its potential use as a photocatalyst in environmental purification and hydrogen generation [1,2]. However, one of the major challenges that hinder the practical application of pristine $TiO_2$-based photocatalytic oxidation is the large band gap of $TiO_2$ (~3.2 eV), which results in the absorption of only UV photons in the solar spectrum. Therefore, the light harvesting of $TiO_2$ in the visible region, which accounts for more than 43% of the total solar energy, should be enhanced [3].

In general, two methods are used to improve light harvesting of $TiO_2$ in the visible region. One involves the sensitization of $TiO_2$ using color centers with appropriate energy levels to promote photoelectron transfer between the color centers and $TiO_2$. A cost-effective sensitization of $TiO_2$ is typically achieved by adding nonmetals such as I [4,5] and S [6,7]. The other method involves decreasing the $TiO_2$ conduction band and/or increasing the valence band by intercalating proper atoms into the $TiO_2$ lattice [8–10].

Another crucial effort is to enhance surface area of $TiO_2$, because the desired photocatalytic reactions occur at the interfaces of the catalyst–pollute solution [10–12]. Intuitively, a plausible approach is to maximize the photoactivity of $TiO_2$ through synthesis of small $TiO_2$ nanoparticles (NPs) that possess a large surface area and a large number of reactive sites. However, reduction in

*Corresponding author at: School of Chemistry and Materials Science, Ludong University, Yantai 264025, China. Tel.: +86 535 6672176; fax: +86 535 6696281.
**Corresponding author. Tel.: +86 531 88364864; fax: +86 531 88574135.
*E-mail addresses:* gaosm@ustc.edu (S. Gao), bbhuang@sdu.edu.cn (B. Huang), bbhuang@sdu.edu.cn (L.R. Grabstanowicz).

0272-8842/$36.00 
http://dx.doi.org/10.1016/j.ceramint.2012.07.021

particle size can introduce more internal crystal defects that act as charge traps, thus diminishing the effective transport of photoinduced charges to the external surface sites, where the desired photocatalytic reaction occurs.

To address these challenges, this study reports a nanoporous AgI/$TiO_2$ composite with AgI color centers. This integral nanoporous composite has less crystal defects but still provides sufficient surface areas for photocatalytic reaction. Synergistically, the selection of AgI as color center also introduces a plasmonic effect, which enhances light harvesting because of localized surface plasmon resonance (LSPR) [13–16]. The spectral position of LSPR and the scattering properties of the AgI NPs depend on the sizes, shapes and composition of NP [17,18].

Thioglycollic acid (TGA) is used as a hydrolysis inhibitor and porosity promoter to produce AgI/$TiO_2$ nanoporous composites. AgI NPs serve as seeds for the nucleation of small $TiO_2$ particles during hydrolyzation. The gaseous species, which result from the decomposition of TGA and unhydrolyzed alkoxyls under heat treatment, can pulverize the $TiO_2$ shell to promote the formation of a nanoporous shell. The resulting porous nanostructure provides more catalytically active centers, and its composition extends the light response of the catalyst into the visible-light region.

## 2. Experimental procedures

### 2.1. Sample preparation

All chemicals used in this study were reagent-grade and obtained from Tianjin Ruijinte Chemical Reagent Co. without further purification. A typical procedure for preparing the porous nanostructures is as follows: 0.06 g KI was first dissolved in 25 mL of 0.2 mol/L aqueous TGA solution. $AgNO_3$ (0.06 g) was then dissolved in 25 mL distilled water, and the $AgNO_3$ solution was added dropwise into the KI–TGA solution with continuous stirring for 0.5 h in the dark at room temperature. AgI–TGA composites were thus formed. Next, 20 mL tetrabutyl orthotitanate [$Ti(OC_4H_9)_4$, TBOT] was dissolved in 40 mL absolute ethyl alcohol, and the solution was stirred for 10 min at ambient temperature to achieve homogeneity. The obtained TBOT solution was then added to the AgI hydrosol at a rate of less than 60 drops/min. During hydrolysis, the liquid was kept under continuous vigorous stirring at room temperature. The resulting suspension was continuously stirred for an additional 2 h at room temperature, and then allowed to stand for 12 h. Finally, the precipitate was filtered out, repeatedly washed with deionized water and absolute ethanol, and oven-dried at 80 °C for 6 h. The precipitate obtained was calcinated in air for 3 h at 300, 400, and 600 °C, respectively, to produce porous nanostructures. The heat-treated samples were denoted as AIT-T, where "-T" indicates the calcination temperatures (in °C). For comparison, pristine $TiO_2$ powder calcinated at 400 °C (denoted as T-400) was also prepared without the addition of the AgI solution.

### 2.2. Sample characterization

The phases of the final products were identified using an X-ray diffractometer (XRD) (Rigaku D/max-2500VPC) with a Ni-filtered Cu Kα radiation at a scanning rate of $0.02^\circ\ s^{-1}$ from 20° to 80°. Sample morphology was observed using a transmission electron microscope (TEM, Hitachi model H800) at an accelerating voltage of 150 kV. Ultraviolet–visible light (UV–vis) diffuse reflection spectra (DRS) were recorded within the range from 200 nm to 800 nm at room temperature using a Shimadzu UV-2550 UV–vis spectrophotometer. The porous structure and Brunauer–Emmett–Teller (BET) surface area were characterized using an $N_2$ adsorption–desorption isotherm (ASAP-2020 Micromeritics Co.). The samples were degassed at 180 °C prior to the BET measurements. The pore volume and pore diameter distributions were derived from the desorption branches of the isotherms in the Barrett–Joyner–Halenda (BJH) model, whereas the BET surface area was calculated from the linear portion of the BET curve. X-ray photoelectron spectra (XPS) were recorded on an X-ray photoelectron spectrometer (VG MicroTech ESCA 3000) using monochromatic $A1_{Ka}$ with a photon energy of 1486.6 eV.

### 2.3. Photocatalytic activity measurements

The photocatalytic activities of the as-prepared porous nanostructures were evaluated by measuring the decomposition rate of methylene blue (MB) at room temperature. The same measurements were also performed on AgI and pristine $TiO_2$ NPs for comparison. The temperature of the photocatalytic reaction was maintained at 30 °C, and visible light was provided by a 300 W tungsten arc lamp (Zhejiang Electric Co., Ltd.) with a glass filter (transparent for $\lambda > 400$ nm). For the photocatalytic experiment, 50 mg AIT–T was added to 150 mL aqueous MB solution ($5.0 \times 10^{-4}$ mol/L) in a custom-made quartz reactor. The concentration of MB solution during the entire experiment was monitored by measuring the UV–vis absorbance. Prior to irradiation, each suspension was magnetically stirred in the dark for 60 min to achieve an adsorption–desorption equilibrium between MB and the photocatalysts. During visible light illumination, approximately 3 mL aliquots were collected from the reaction solution at 10 min intervals and centrifuged to remove trace particles. The absorbance of the centrifuged solutions was then measured in the range from 500 nm to 800 nm.

## 3. Results and discussion

### 3.1. XRD characterization of the crystal structure

The porous nanostructures were prepared via the hydrolysis of TBOT in a TGA-coated AgI hydrosol, followed by 3 h heat treatment in air at elevated temperatures. Powder XRD was used to monitor the changes in the structure and crystallite sizes of the prepared porous nanostructures at different temperatures. Fig. 1 shows the XRD patterns of

the samples before and after heat treatment at different temperatures (300 °C to 600 °C). Prior to thermal treatment, the samples appear as an amorphous $TiO_2$ phase. This result is attributed to the relatively incomplete hydrolysis of TBOT at room temperature, which causes large amounts of unhydrolyzed alkyls to remain in the xerogel powders. As a result, adsorption of unhydrolyzed alkyls onto the surface of the $TiO_2$ particles prevents further crystallization of $TiO_2$ [19].

After heat treatment, the patterns show the formation of anatase $TiO_2$. As the annealing temperature increases, the peaks assigned to the anatase phase become sharper and more intense because of the formation of larger grains, as summarized in Table 1. The average crystallite sizes of the AIT-300, AIT-400, and AIT-600 AgI/$TiO_2$ porous composites are 4.7, 7.6, and 14.5 nm, respectively; these values were estimated from the full-width at half-maximum of the diffraction peaks using the Scherrer equation. No peaks corresponding to AgI were observed in the XRD patterns, indicating its low content and small particle size.

### 3.2. UV–vis diffuse reflectance spectra

Fig. 2 shows the UV–vis DRS spectra of the prepared AIT–T samples, pristine T-400, and AgI. Compared with the spectra for pristine T-400 and AgI, the spectra of the AIT–T samples show a strong broad absorption band between 400 nm and 800 nm, which covers the entire visible range. An enhancement of the absorption intensity was also observed, and the absorption peak at ~425 nm is assigned to the direct band gap of AgI [20]. Pure $TiO_2$ has no adsorption in the visible-light region; therefore, the absorption edge is attributed to AgI. AIT-400 showed the maximum absorption within the visible region compared with the other samples. The absorption spectra of the AIT-300 and AIT-400 samples are similar because of the composite results of AgI and $TiO_2$. However, at 600 °C, a broad absorption covering the 450–800 nm range with a summit at ~540 nm appears. This phenomenon is attributed to the plasma resonance effect of the metallic silver NPs [21–23], indicating that the core AgI NPs decompose at 600 °C, generating Ag metal and resulting in the plasma effect. Therefore, the annealing temperature is an important parameter that determines the nanostructures and photocatalytic properties of the composites.

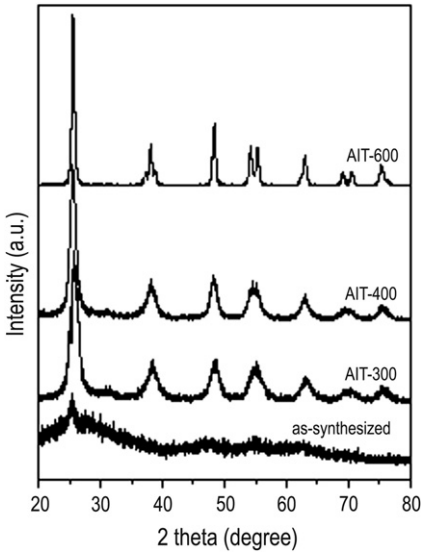


Fig. 1. X-ray diffraction (XRD) patterns of the as-synthesized precursor and the AIT-T composites after calcination at 300, 400, and 600 °C.

### 3.3. X-ray photoelectron spectra (XPS)

The UV–vis DRS spectra indicate that the core AgI NPs decomposed into metal Ag at 600 °C. The chemical states of Ag and I were then examined via XPS. Fig. 3(a) and (b) shows the high-resolution XPS spectra of Ag 3*d* and I 3*d* for samples AIT-400 and AIT-600, respectively. The Ag 3*d* spectrum of AIT-400 consists of two individual peaks at 367.6 and 373.5 eV, which can be attributed to the Ag $3d_{5/2}$ and Ag $3d_{3/2}$ binding energies, respectively, and are assigned

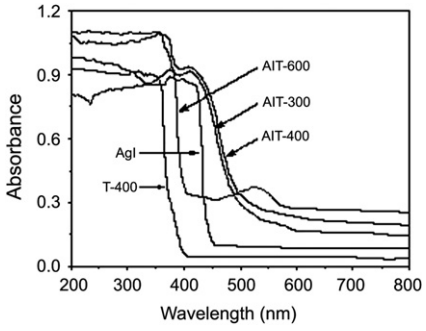


Fig. 2. Ultraviolet–visible light diffuse reflectance spectra of AIT-T catalysts at different calcination temperatures compared with AgI and pristine T-400.

Table 1
Physicochemical properties of AIT samples and pristine $TiO_2$ from $N_2$ sorption analysis and XRD results[a].

| Sample | $S_{BET}$ ($m^2$/g) | Pore volume ($cm^3$/g) | Average pore size (nm) | Crystal size (nm) |
|---|---|---|---|---|
| AIT-300 | 198.70 | 0.387 | 37.068 | 4.7 |
| AIT-400 | 139.79 | 0.312 | 37.390 | 7.6 |
| AIT-600 | 61.60 | 0.112 | 30.007 | 14.5 |
| T-400 | 51.8 | 0.104 | 26.341 | 6.8 |

[a]BET surface areas were calculated by the multipoint BET method from the linear part of the BET plots. Single point absorption total pore volumes were obtained from the volume of $N_2$ adsorbed at $P/P_0$=0.995. Average pore diameters were estimated using the desorption branch of the isotherm and the BJH formula. Crystal size was determined from the XRD pattern using the Scherrer equation.

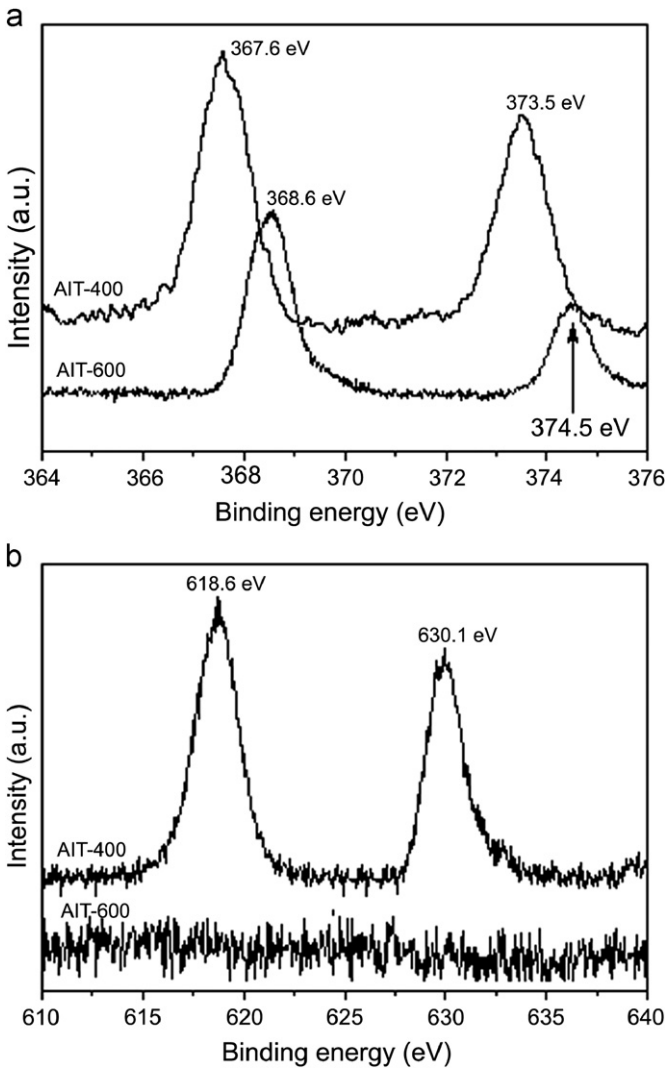


Fig. 3. High-resolution X-ray photoelectron spectroscopy (XPS) of Ag 3*d* (a) and I 3*d* (b) patterns for AIT-400 and AIT-600.

to $Ag^+$ of AgI [24]. For the AIT-600 sample, the binding energies are 368.6 and 374.5eV, indicating the presence of metal $Ag^0$ [25]. The XPS spectrum of the I 3*d* region of AIT-400 shows doublet peaks at 618.6 eV (I $3d_{3/2}$) and 630.1 eV (I $3d_{5/2}$), which are assigned to $I^-$ in AgI [18]. No I was found at 600 °C, indicating that the synthesized AgI/$TiO_2$ nanostructures are stable at low temperatures. However, the core AgI NPs decomposed and generated metal Ag and $I_2$ when the calcination temperature reached 600 °C. AgI/$TiO_2$ nanostructures converted into Ag/$TiO_2$ nanostructures due to the sublimation of elemental $I_2$.

### 3.4. TEM characterization of particle morphology

The morphologies of the precursor of AgI/$TiO_2$ and the nanostructures after calcination at 300, 400, and 600 °C were characterized via TEM Fig. 4(a), (b), (c) and (d), respectively). After TBOT was hydrolyzed in the AgI hydrosol, the newly formed particles showed an average size of about 150 nm (Fig. 4(a)); no porous structure was observed at this stage. The subsequent heat treatment resulted in the formation of mesoporous structures, as shown in Fig. 4(b)–(d). Each individual sphere consists of a large number of tiny and loosely packed $TiO_2$ NPs (approximately 4–8 nm in diameter), which are called primary NPs. As a result, the interstitial voids between these primary NPs constitute a short-range disordered nanoporous structure, which is called primary nanopores. In comparison, the voids between the large spheres (termed secondary NPs) also create pores, which are called secondary nanopores [4,6]. The morphology of the primary pores gradually changes as the size of the primary NPs increases with increasing heat treatment temperature.

### 3.5. BET measurement of the specific surface area and pore size distribution

The pore size and specific surface area (SSA) of the samples were further characterized via nitrogen adsorption–desorption isotherm measurements. Fig. 5 shows the nitrogen adsorption–desorption and BJH desorption isotherms. The results indicate a hierarchically bimodal pore-size distribution in the mesoporous and macroporous regions of AIT-300 and AIT-400 [26]. The first hysteresis loops for samples AIT-300 and AIT-400, locating at a relatively low pressure ($0.4 < P/P_0 < 0.7$), are associated with the framework-confined primary nanopores consisting of interstitial voids between the smaller NPs. The shape and position of these loops are slightly different, depending on heat treatment temperatures. The first loop for AIT-300 is located at $0.4 < P/P_0 < 0.5$, whereas for AIT-400 it is located at $0.4 < P/P_0 < 0.65$. The monolayer adsorption for AIT-300 and AIT-400 is complete when the relative pressure reaches 0.5 and 0.65, respectively, indicating that AIT-400 has a larger primary pore size than AIT-300. The second hysteresis loop located at $0.85 < P/P_0 < 1.0$ is related to secondary pores composed of the voids among large secondary particles [27]. For AIT-600, the hysteresis loops located at $0.6 < P/P_0 < 0.8$ indicate that AIT-600 has the largest primary pore size compared with AIT-300 and AIT-400. The observed hysteresis loops for AIT-300 and AIT-400 approach $P/P_0 = 1$, suggesting the presence of macropores [28].

The BJH desorption isotherm results (Fig. 5, inset) suggest that samples AIT-300 and AIT-400 show a bimodal pore-size distribution consisting of smaller primary pores and larger secondary pores. The smaller pores reflect the porosity within the $TiO_2$ shells, whereas the larger pores are related to the pores formed between aggregated AgI/$TiO_2$ nanostructures. For AIT-600, only one smaller pore-size distribution is observed, indicating the fusion of the primary NPs at high temperature. This result is consistent with those of TEM.

Table 1 summarizes the physical properties of the porous nanostructure samples obtained after calcination at various temperatures, as well as that of pristine T-400. The pore volume and SSA decreased with increasing calcination

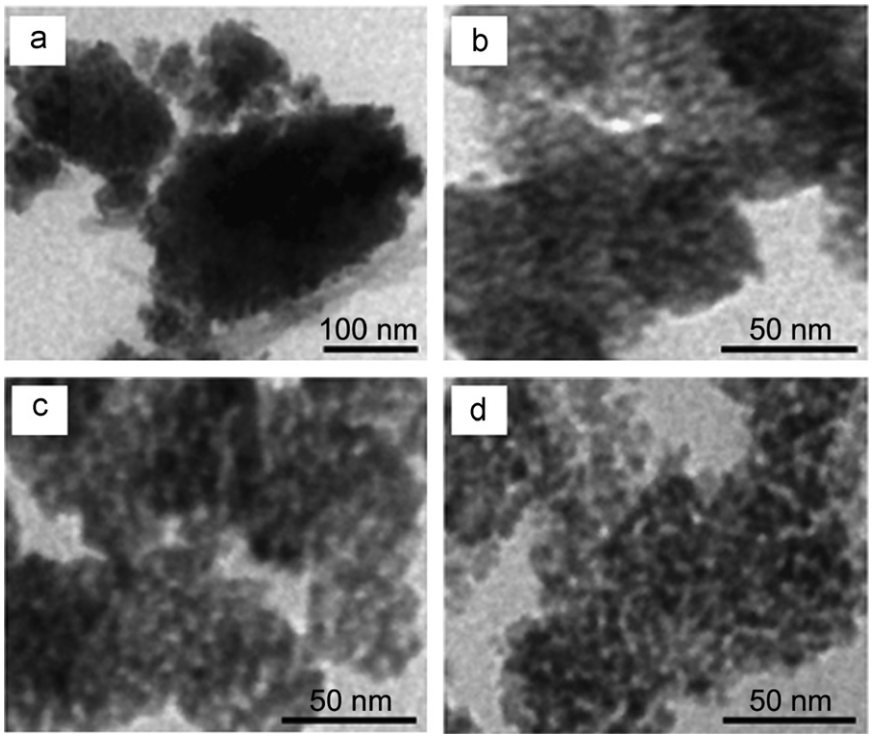


Fig. 4. Transmission electron microscopy (TEM) images of (a) the AgI/$TiO_2$ precursor and the obtained porous nanostructures after thermal treatment at (b) 300, (c) 400, and (d) 600 °C.

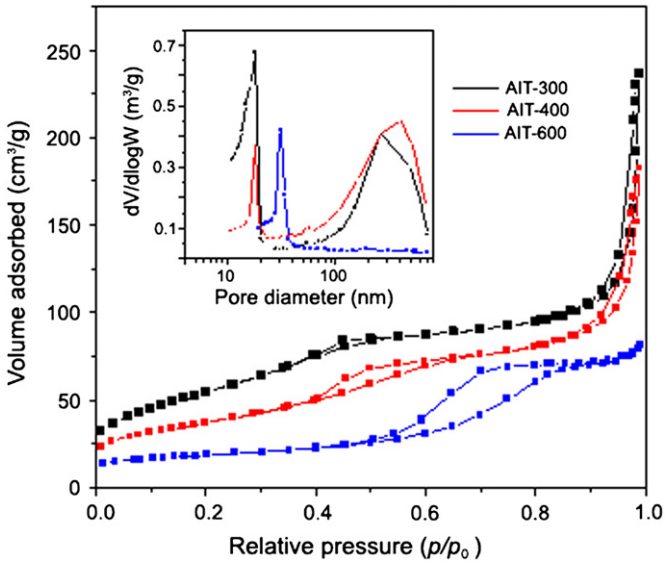


Fig. 5. $N_2$ adsorption–desorption isotherms and the corresponding Barrett–Joyner–Halenda (BJH) pore size distributions of the as-prepared AIT samples.

temperatures. AIT-300 exhibits a wide BET surface area of 198 $m^2 g^{-1}$ and a high pore volume of 0.386 $cm^3 g^{-1}$. Although the BET surface area of AIT-600 decreased to 61.6 $m^2 g^{-1}$, it is still larger than that of commercial P25 $TiO_2$ (~50 $m^2 g^{-1}$) and pristine $TiO_2$. These porous structures possessing high specific surface area are of particular interest because they can provide abundant active sites for the adsorption of pollutant molecules. This feature can enhance the catalytic activity as indicated in the measurement of the photocatalytic activity on MB degradation.

### 3.6. Proposed formation mechanism of the porous composites

A multistep mechanism (Fig. 6) is proposed to explain the formation of the AgI/$TiO_2$ or Ag/$TiO_2$ porous nanostructures. TGA plays an important role in porous nanostructure formation by acting as a pore-forming agent, hydrolysis inhibitor, and ligand for the titanium complexes. During the reaction of $AgNO_3$ and KI, mercaptan anions attach to the AgI surface through mercapto groups; silver mercaptan molecular complex also exists as a result of competitive reactions [29]. Two different surface structures of mercaptan-modified AgI particles are assumed (Fig. 6). One assumes that all $Ag^+$ sites on the AgI particle surface are occupied by adsorbed mercaptan, and that the entire surface $I^-$ sites are covered by $Ag^+$ ions to compensate for the excess negative charges caused by the adsorbed $RS^-$ ions. The other assumes that the largest coverage of mercaptan is on the AgI surface because all $Ag^+$ sites are bound to the $RS^-$ ions [29,30]. On the other hand, TGA can effectively suppress the hydrolysis rates of TBOT in the aqueous solution. An acid is usually used to delay the hydrolysis rates, which determines the synthesis pathway and affects the micro–nanostructure of the inorganic species. So, acids appear to be important in the formation of the mesophases of oxides [31].

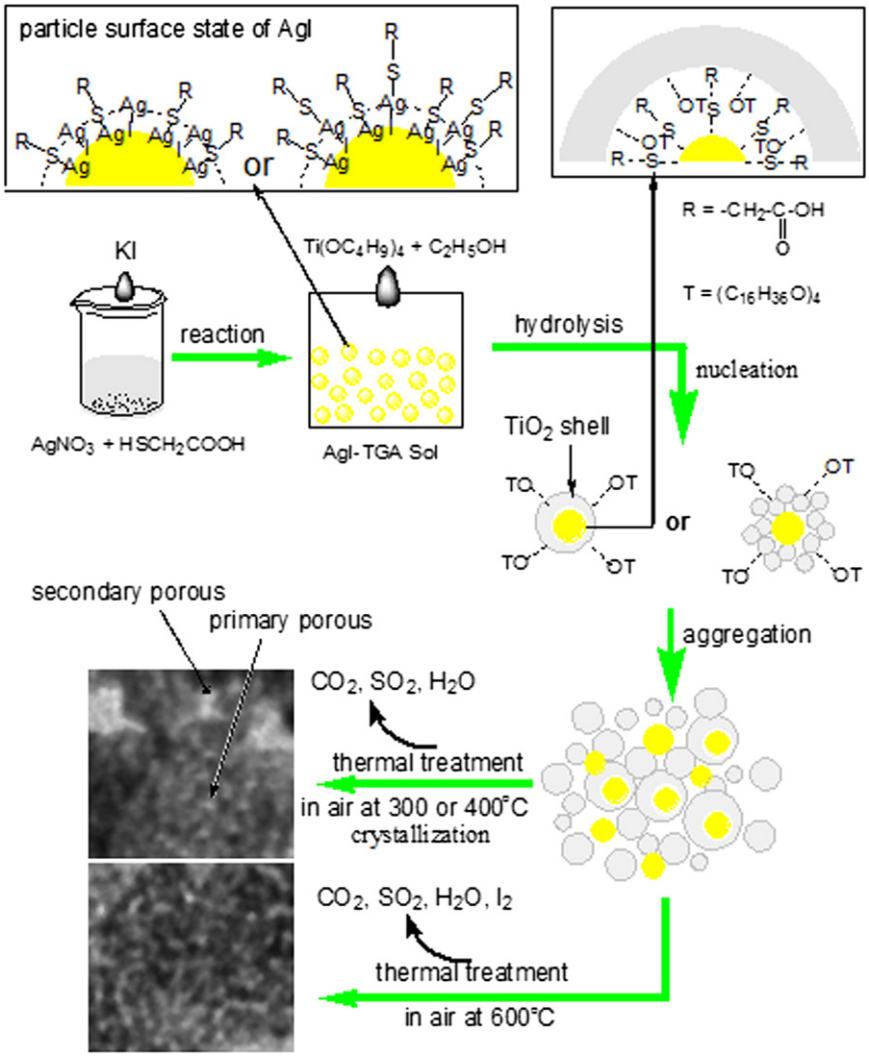


Fig. 6. Schematic diagram of the formation mechanisms of the AgI/$TiO_2$ and Ag/$TiO_2$ porous nanostructures.

When TBOT was added to the mercaptan-coated AgI hydrosol, the $Ti(OBu)_4$ molecules were adsorbed onto the surface of the AgI NPs and slowly hydrolyzed to become a titania precursor layer on the AgI NPs. These primary $TiO_2$ particles formed as a shell on the surface of the AgI particles, which in turn become nucleation sites for $TiO_2$ spheres via TBOT hydrolysis. This phenomenon is confirmed by the TEM images in Fig. 4(a).

The hydrolysis of TBOT at room temperature and in acidic conditions is relatively slow and incomplete. Therefore, a large amount of unhydrolyzed alkoxyls still remains in the xerogel powders [32]. The subsequent heat treatment of the xerogel at elevated temperatures has led to a series of reactions between the mercaptan, alkyls, AgI, and amorphous $TiO_2$ in the presence of $O_2$. When the precursor is calcinated at relatively lower temperatures (300 and 400 °C), the organics within the powder are oxidized into $CO_2$, $SO_2$, and $H_2O$. The resulting gaseous products pulverize the $TiO_2$ shell, thereby forming the primary pores. Concurrently, the amorphous $TiO_2$ crystallizes into anatase $TiO_2$, and the aggregation of the secondary particles results in the formation of secondary pores, consisting of voids among the secondary particles during heat treatment. At 600 °C, the core AgI NPs decomposes into metal Ag, $I_2$ and elemental $I_2$ sublimates and escapes, whereas most mesoporous structures collapse and form new Ag/$TiO_2$ porous nanostructures.

### 3.7. Photocatalytic activity in methylene blue decomposition

MB is a brightly colored blue cationic thiazine dye, which is often used as a test model pollutant in semiconductor photocatalysis. Fig. 7(a) shows the adsorption and photodegradation ability of the AIT-T samples against MB solutions in comparison with those of pristine $TiO_2$ (T-400) and pure AgI. A blank experiment was also performed. The pure MB solution does not decompose without a catalyst. Prior to turning the light on, the MB concentrations are depleted faster in the presence of the AIT-T samples than in T-400 and pure AgI. This effect is attributed to the larger surface area of the AIT-T samples. The adsorption capacity of AIT-T increases with the

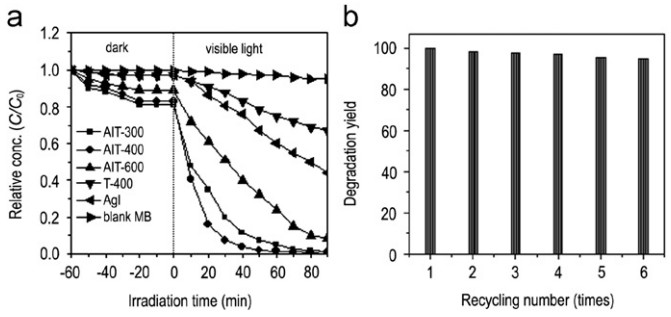


Fig. 7. (a) Blank MB solution, adsorption and photodegradation of MB solutions using pristine T-400, AgI, and AIT-T samples as photocatalysts under visible-light irradiation in neutral suspension. (b) Recycling test results for the AIT-400 sample.

decrease in heat treatment temperatures due to the reduced surface area.

Fig. 7(a) shows that the MB solutions containing AIT-300 and AIT-400 undergo significant degradation and become nearly transparent within 50 min under visible-light illumination. AIT-400 exhibits the best photocatalytic activity. By contrast, the MB solution containing T-400 shows very limited degradation. The AIT-600 sample has positive photocatalytic properties resulting from the plasma effect; however, these properties are inferior to those of AIT-300 and AIT-400 because of its smaller specific surface. Meanwhile, the photocatalytic performance of pure AgI gradually increases when the illumination time is increased because of the decomposition of pure AgI under light, as well as partial decomposition of AgI NPs, which generates metal Ag. These metal Ag particles attach to the surface of the AgI particle, resulting in the surface plasmon resonance effect, which, in turn, results in improved photocatalytic performance. Plasmonic photocatalysts are based on the localized surface plasmon resonance (LSPR) of the noble metal, metal–semiconductor contact, and semiconductor photocatalysts [16]. Pure AgI are unstable under light irradiation. However, metal Ag on the surface of Ag/AgI scavenges $h^+_{VB}$ and then traps $e^-_{CB}$ in the process of the photocatalytic reaction, inhibiting the decomposition of AgI and reducing the recombination rate of the electron–hole pair [33]. So the LSPR of metal Ag NPs for degrading MB is larger than that of pure AgI NPs.

The BET results indicate that AIT-300 has the largest surface area; however, it does not have the highest photocatalytic property, which is often due to a small particle size or a porous structure and corresponds to low anatase crystallinity. Low anatase crystallinity indicates the presence of too many defects, which further promotes the recombination of the photogenerated electrons and holes [34]. The surface area of AIT-400 is larger, and its anatase crystallinity is better than those of AIT-300 (Figs. 1 and 5 and Table 1), suggesting that AIT-400 has higher anatase crystallinity and fewer defects compared with AIT-300. Therefore, AIT-400 has the highest photocatalytic oxidation activity against MB.

The stability of a photocatalyst is highly important for its application. The stability of AIT-400 was investigated via repeated recycling in MB bleaching experiments. No significant decrease in the photocatalytic oxidation activity is observed after six cycles of usage (Fig. 7(b)), making AIT-400 very promising for practical application.

The photocatalytic activity of the powders can be quantitatively evaluated by comparing their apparent reaction rate constants. The photocatalytic oxidation of organic pollutants in aqueous suspensions follows the Langmuir–Hinshelwood model [35,36], which is described as [27]

$$\ln\left(\frac{C_0}{C_t}\right) = k_{app}t$$

where $C_t$ is the concentration of aqueous MB at reaction time $t$, $C_0$ is the initial MB concentration, $k_{app}$ is the apparent rate constant, and $t$ is the reaction time. The variations in $\ln(C_0/C)$ as a function of the irradiation time are given in Fig. 8. All the curves can be fitted roughly to a straight line. Thus, the photocatalytic degradation reaction is assumed to follow first-order kinetics [37]. The rate constants for the photodegradation of MB using the AIT-400 and AIT-300 nanoporous composites are 16.3 and 11.0 times higher than that of pure $TiO_2$ and 8.8 and 5.9 times higher than AgI, respectively. Therefore, the AIT-400 and AIT-300 nanoporous composites exhibit strong photocatalytic activity for MB decomposition under visible-light irradiation.

The highly efficient visible light photocatalytic activity of the nanostructured AgI/$TiO_2$ or Ag/$TiO_2$ are attributed to its strong absorption in the visible region and low recombination rate of the electron–hole pair due to the synergetic effect among the components of AgI, Ag, and $TiO_2$ in the nanostructure. Once a composite of AgI and $TiO_2$ is formed, AgI can be excited by visible light and generate electron–hole pairs. Metal Ag on the surface of the nanostructures acts as electron traps, resulting in a stabilization of electron–hole

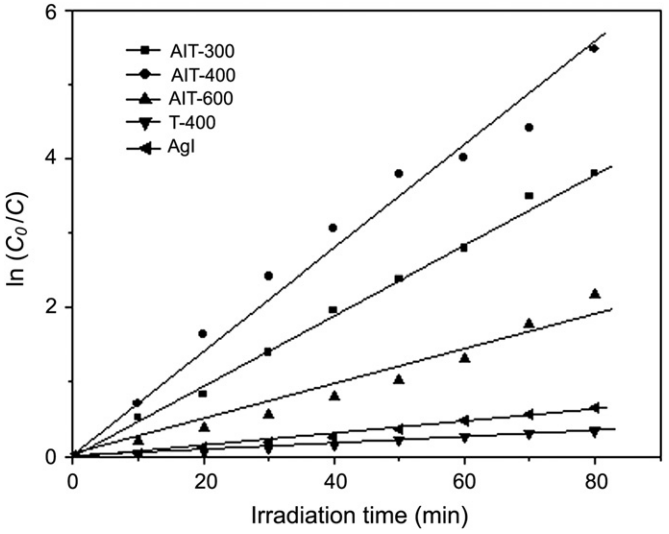


Fig. 8. Variation in the normalized $\ln(C_0/C)$ of the MB concentration as a function of visible-light irradiation time.

pairs and electron migration from the conduction band of AgI to that of $TiO_2$ [18,38,39].

## 4. Conclusions

AgI/$TiO_2$ and AgI/$TiO_2$ porous nanostructures with high crystallinity and high surface area have been synthesized through a hydrolysis–calcination process. The AgI–TGA NPs serve as seeds and TGA is used as a hydrolysis inhibitor and porosity promoter. The calcination temperatures affect composition and porosity of the nanostructures. AgI/$TiO_2$ porous nanostructures are formed at low calcination temperatures (300 and 400 °C). On the other hand, Ag/$TiO_2$ porous nanostructures appear when the calcination temperature reaches 600 °C. The different porous nanostructures obtained exhibit an enhanced visible light-driven photocatalytic oxidation activity against MB, which is attributed to the high specific surface area of the porous nanostructures and the high absorbance in the visible-light range. The architecturally controllable morphology of the $TiO_2$ nanostructure composite presented in this work provides a novel method for further enhancing the visible-light-driven photooxidation of organic pollutants.

## Acknowledgments

S.M.Gao and B.B.Huang thank the National Basic Research Program of China (973 Program, no. 2007CB 613302), A Project of Shandong Province Higher Educational Science and Technology Program (J12LA01). T.X. acknowledges the financial support from NIU Summer Research and Artistry Grant.

## References

[1] X.B. Chen, S.H. Shen, L.J. Guo, S.S. Mao, Semiconductor-based photocatalytic hydrogen generation, Chemical Reviews 110 (2010) 6503–6570.
[2] A. Kubacka, M.F. García, G. Colón, Advanced Nanoarchitectures for solar photocatalytic applications, Chemical Reviews 112 (2012) 1555–1614.
[3] M.P. Seabra, I.M. Miranda Salvado, J.A. Labrincha, Pure and (zinc or iron) doped titania powders prepared by sol–gel and used as photocatalyst, Ceramics International 37 (2011) 3317–3322.
[4] P. Xu, J. Lu, T. Xu, S.M. Gao, B.B. Huang, Y. Dai, $I_2$–hydrosol-seeded growth of $(I_2)_n$–C-codoped meso/nanoporous $TiO_2$ for visible light-driven photocatalysis, Journal of Physical Chemistry C 114 (2010) 9510–9517.
[5] S. Usseglio, A. Damin, D. Scarano, S. Bordiga, A. Zecchina, C. Lamberti, $(I_2)_n$ encapsulation inside $TiO_2$: a way to tune photoactivity in the visible region, Journal of the American Chemical Society 129 (2007) 2822–2828.
[6] P. Xu, T. Xu, J. Lu, S.M. Gao, N.S. Hosmane, B.B. Huang, Y. Dai, Y.B. Wang, Visible-light-driven photocatalytic S- and C-codoped meso/nanoporous $TiO_2$, Energy and Environmental Science 3 (2010) 1128–1134.
[7] H. Tian, J.F. Ma, K. Li, J.J. Li, Hydrothermal synthesis of S-doped $TiO_2$ NPs and their photocatalytic ability for degradation of methyl orange, Ceramics International 35 (2009) 1289–1292.
[8] S. Sakthivel, H. Kisch, Daylight photocatalysis by carbon-modified titanium dioxide, Angewandte Chemie—International Edition 42 (2003) 4908–4911.
[9] J. Wang, D.N. Tafen, J.P. Lewis, Z. Hong, A. Manivannan, M. Zhi, M. Li, N. Wu, Origin of photocatalytic activity of nitrogen-doped $TiO_2$ nanobelts, Journal of the American Chemical Society 131 (2009) 12290–12297.
[10] R. Asahi, T. Morikawa, T. Ohwaki, K. Aoki, Y. Taga, Visible-light photocatalysis in nitrogen-doped titanium oxides, Science 293 (2001) 269–271.
[11] V. Loryuenyong, K. Angamnuaysiri, J. Sukcharoenpong, A. Suwannasri, Sol–gel derived mesoporous titania NPs: effects of calcination temperature and alcoholic solvent on the photocatalytic behavior, Ceramics International 38 (2012) 2233–2237.
[12] Z.K. Zheng, B.B. Huang, X.Y. Qin, X.Y. Zhang, Y. Dai, Strategic synthesis of hierarchical $TiO_2$ microspheres with enhanced photocatalytic activity, Chemistry—A European Journal 16 (2010) 11266–11270.
[13] H.F. Cheng, B.B. Huang, P. Wang, Z.Y. Wang, Z.Z. Lou, J.P. Wang, X.Y. Qin, X.Y. Zhang, Y. Dai, *In situ* ion exchange synthesis of the novel Ag/AgBr/BiOBr hybrid with highly efficient decontamination of pollutants, Chemical Communications 47 (2011) 7054–7056.
[14] P. Wang, B.B. Huang, X.Y. Qin, X.Y. Zhang, Y. Dai, J. Wei, M.H. Whangbo, Ag@AgCl: a highly efficient and stable photocatalyst active under visible light, Angewandte Chemie—International Edition 47 (2008) 7931–7933.
[15] P. Wang, B.B. Huang, Z.Z. Lou, X.Y. Zhang, X.Y. Qin, Y. Dai, Z.K. Zheng, X.N. Wang, Synthesis of high efficient plasmon photocatalyst Ag@AgCl with various structures, Chemistry–A European Journal 16 (2010) 538–544.
[16] P. Wang, B.B. Huang, X.Y. Zhang, X.Y. Qin, Y. Dai, Z.Y. Wang, Z.Z. Lou, Highly efficient visible light plasmonic photocatalysts Ag@Ag(Cl,Br) and Ag@AgCl–AgI, ChemCatChem 3 (2011) 360–364.
[17] C. Hu, T.W. Peng, X.X. Hu, Y.L. Nie, X.F. Zhou, J.H. Qu, H. He, Plasmon-induced photodegradation of toxic pollutants with Ag–AgI/$Al_2O_3$ under visible-light irradiation, Journal of the American Chemical Society 132 (2010) 857–862.
[18] Y. Li, Z.H. Zhang, Z.M. Guo, J.J. Han, X.J. Zhao, Q.N. Zhao, S.J. Kim, Highly efficient visible-light-induced photocatalytic activity of nanostructured AgI/$TiO_2$ photocatalyst, Langmuir 24 (2008) 8351–8357.
[19] J.G. Yu, J.C. Yu, W.K. Ho, M.K.P. Leung, B. Cheng, G.K. Zhang, X.J. Zhao, Effects of alcohol content and calcination temperature on the textural properties of bimodally mesoporous yitania, Applied Catalysis A—Chemical. 255 20030 pp. 309–320.
[20] D. Fitzmaurice, H. Frei, J. Rabani, Time-resolved optical study on the charge carrier dynamics in a $TiO_2$/AgI sandwich colloid, Journal of Physical Chemistry 99 (1995) 9176–9181.
[21] L.B. Yang, X. Jiang, W.D. Ruan, J.X. Yang, B. Zhao, W.Q. Xu, J.R. Lombardi, Charge-transfer-induced surface-enhanced raman scattering on Ag–$TiO_2$ nanocomposites, Journal of Physical Chemistry C 113 (2009) 16226–16231.
[22] Z.K. Zheng, B.B. Huang, X.Y. Qin, X.Y. Zhang, Y. Dai, M.–H. Whangbo, Facile in situ synthesis of visible-light plasmonic photocatalysts M@$TiO_2$ (M=Au, Pt, Ag) and evaluation of their photocatalytic oxidation of benzene to phenol, Journal of Materials Chemistry 21 (2011) 9079–9087.
[23] S. Rengaraj, X.Z. Li, Enhanced photocatalytic activity of $TiO_2$ by doping with Ag for degradation of 2,4,6-trichlorophenol in aqueous suspension, Journal of Molecular Catalysis A—Chemical 243 (2006) 60–67.
[24] M.R. Elahifard, S. Rahimnejad, S. Haghighi, M.R. Gholami, Apatite-coated Ag/AgBr/$TiO_2$ visible-light photocatalyst for destruction of bacteria, Journal of the American Chemical Society 129 (2007) 9552–9553.
[25] J.G. Yu, G.P. Dai, B.B. Huang, Fabrication and characterization of visible-light driven plasmonic photocatalyst Ag/AgCl/$TiO_2$ nanotube arrays, Journal of Physical Chemistry C 113 (2009) 16394–16401.

[26] K.–N.P. Kumar, J. Kumar, K. Keizer, Effect of peptization on densification and phase-transformation behavior of sol–gel-derived nanostructured titania, Journal of the American Ceramic Society 77 (1994) 1396–1400.
[27] J.G. Yu, G.H. Wang, B. Cheng, M.H. Zhou, Effects of hydrothermal temperature and time on the photocatalytic activity and microstructures of bimodal mesoporous $TiO_2$ powders, Applied Catalysis B—Environmental 69 (2007) 171–180.
[28] D.V. Bavykin, V.N. Parmon, A.A. Lapkin, F.C. Walsh, The effect of hydrothermal conditions on the mesoporous structure of $TiO_2$ nanotubes, Journal of Materials Chemistry 14 (2004) 3370–3377.
[29] S.H. Chen, T. Ida, K. Kimura, Thiol-derivatized AgI NPs: synthesis, characterization, and optical properties, Journal of Physical Chemistry B 102 (1998) 6169–6176.
[30] S.H. Chen, X.M. Ren, S.X. Ji, X-ray and auger photoelectron spectroscopic characterization of silver surface treated in 2-mercaptobenzothiazole solution, Journal of Information Recording Materials 20 (1993) 359–373.
[31] J. Aguado-Serrano, M.L. Rojas-Cervantes, Titania aerogels: influence of synthesis parameters on textural, crystalline, and surface acid properties, Microporous and Mesoporous Materials 88 (2006) 205–213.
[32] J.G. Yu, M.H. Zhou, B. Cheng, H.G. Yu, X.J. Zhao, Ultrasonic preparation of mesoporous titanium dioxide nanocrystalline photocatalysts and evaluation of photocatalytic activity, Journal of Molecular Catalysis A—Chemical 27 (2005) 75–80.
[33] C. Hu, X.X. Hu, L.S. Wang, J.H. Qu, A.M. Wang, Visible-light-induced photocatalytic degradation of azodyes in aqueous $AgI/TiO_2$ dispersion, Environmental Science and Technology 40 (2006) 7903–7907.
[34] G.H. Tian, H.G. Fu, L.Q. Jing, B.F. Xin, K. Pan, Preparation and characterization of stable biphase $TiO_2$ photocatalyst with high crystallinity, large surface area, and enhanced photoactivity, Journal of Physical Chemistry C 112 (2008) 3083–3089.
[35] J.H. Sun, X.L. Wang, J.Y. Sun, R.X. Sun, S.P. Sun, L.P. Qiao, Photocatalytic degradation and kinetics of orange G using nanosized $Sn(IV)/TiO_2$/AC photocatalyst, Journal of Molecular Catalysis A—Chemical 260 (2006) 241–246.
[36] C. Wu, H. Chang, J. Chen, Basic dye decomposition kinetics in a photocatalytic slurry reactor, Journal of Hazardous Materials B 137 (2006) 336–343.
[37] J.M. Wu, T.W. Zhang, Photodegradation of rhodamine B in water assisted by titania films prepared through a novel procedure, Journal of Photochemistry and Photobiology A 162 (2004) 171–177.
[38] H. Tada, K. Teranishi, Y. Inubushi, S. Ito, $TiO_2$ photocatalytic reduction of bis (2-dipyridyl) disulfide to 2-mercaptopyridine by $H_2O$: incorporation effect of nanometer-sized Ag particles, Chemical Communications 21 (1998) 2345–2346.
[39] F. Donald, F. Heinz, R. Joseph, Time-resolved optical study on the charge carrier dynamics in a $TiO_2$–AgI sandwich colloid, Journal of Physical Chemistry 99 (1995) 9176–9181.